International Journal of Heat and Mass Transfer 52 (2009) 1573–1581

Contents lists available at ScienceDirect

International Journal of Heat and Mass Transfer

journal homepage: www.elsevier.com/locate/ijhmt

Turbulence modeling for flow in a distribution manifold

Andrew Chen [a], Ephraim M. Sparrow [b,*]

[a] Engineering Analysis Group, 3M Company, St. Paul, MN 55144, USA
[b] Mechanical Engineering Department, Heat Transfer Laboratory, University of Minnesota-Twin Cities, 125 MEB, 111 Church Street, Minneapolis, MN 55455, USA

ARTICLE INFO

Article history:
Received 22 September 2007
Received in revised form 9 August 2008
Available online 15 October 2008

Keywords:
Turbulence model
Distribution manifolds
Exit port array
Pipe flow
CFD
Numerical simulation

ABSTRACT

An investigation of candidate turbulence models for application to the flow in a distribution manifold has been performed by a synergistic combination of numerical simulation and laboratory experiments. The investigated manifold was a cylindrical chamber fitted with an array of discharge slots deployed axially and uniformly along the length of the chamber. Three turbulence models were considered for the numerical simulations: standard k–ϵ, renormalized group k–ϵ (RNG), and realizable k–ϵ (REAL). The numerical predictions obtained from the application of these models were compared with the experimental results, and the REAL model was found to provide the best representation of the data. Special attention was given to the pressure variation along the length of the manifold, the per-exit-slot mass discharge, and the angle at which the exiting mass leaves the manifold. The departure angle is related to the axial momentum carried by the exiting flow. As confirmed by both the numerical simulations and the experiments, the departure angles varied from 68 to 90° from the upstream end to the downstream end of the manifold (90° is perpendicular to the axis). An in-depth study of numerical accuracy was performed encompassing number of nodes, deployment of nodes, and positioning of the solution domain.

1. Introduction

Manifolds are a frequently encountered component in a wide spectrum of heat transfer and flow fluid devices. A distribution manifold is a chamber which receives fluid through a single inlet and disperses the fluid through multiple exits. In contrast, a collection manifold receives fluid through multiple inlets and discharges the fluid though a single exit. Often, in practice, a distribution manifold and a collection manifold may be paired to form a single unit. The pattern of fluid flow in a manifold is highly complex. For instance, in a distribution manifold, the flow encounters a sequence of branch points at the successive exit ports. The axial momentum carried by the main flow diminishes along the length of the manifold as the flow is depleted. Transverse velocities are induced to feed the outflows at the exit ports, and the main flow never achieves a fully developed state. Furthermore, in practice, the manifold flow is likely to be turbulent.

Numerical simulation by means of computational fluid dynamics is the current method of choice for solving the manifold problem, as witnessed by a review of the published literature. A representative sample of publications conveying current practice for CFD modeling of turbulent flow in manifolds and related geometries may be found in references [1–13]. An interesting feature of the current practice is an incomplete approach to the selection of a suitable turbulence model. There is a substantial number of candidate turbulence models available in the literature which are conveniently offered to users of commercial software. None of the available models can be regarded as being applicable to the totality of turbulent flows. When highly complex flows are simulated, special care is needed to identify the best of the available models.

It is widely accepted that the most convincing method for choosing the most suitable among the available turbulence models is by comparison of the model-based predictions with relevant experimental data. In implementing this approach, it is reasonable to consider several likely turbulence models for assessment. This path has been followed here along with careful experimentation to obtain the data needed for the selection process.

The aforementioned selection process has not been closely followed in the published literature as cited in the penultimate paragraph. With one exception [9], only a single turbulence model was considered in each investigation. The favored model is k–ϵ, which is the first of the two-equation models [14]. In [9], two turbulence models were employed but without comparisons with experimental data.

The manifold system to be studied here is intended to simulate one that occurs commonly in industrial processing equipment. A schematic diagram of the studied manifold is presented in Fig. 1. The figure shows a multi-port, cylindrical distribution manifold supplied with air from an upstream pipe whose internal diameter is identical to that of the manifold. The upstream pipe functions as a hydrodynamic development length. Thirty-nine exit ports

* Corresponding author. Tel.: +1 612 625 5022; fax: +1 612 625 5230.
E-mail address: esparrow@umn.edu (E.M. Sparrow).

0017-9310/$ - see front matter © 2008 Elsevier Ltd. All rights reserved.
doi:10.1016/j.ijheatmasstransfer.2008.08.006

Nomenclature

C_μ	empirical constant in Eq. (9)
D	internal diameter
f	friction factor, Eq. (1)
k	turbulence kinetic energy
L	radial distance from outer surface of manifold
m^*_{avg}	total mass flow rate divided by number of slots
m^*_{slot}	per-slot mass flow rate
n	slot number
p	pressure
p_{amb}	pressure in the ambient
Re	Reynolds number, Eq. (3)
U	mean velocity
U_{max}	maximum velocity in the pipe cross-section
u	velocity component in the x-direction
v	velocity component in the y-direction
W	slot width
w	velocity component in the z-direction
x	axial coordinate
y	transverse coordinate
z	transverse coordinate

Greek symbols

ε	turbulence dissipation rate
μ	viscosity
μ_{eff}	effective viscosity (laminar plus turbulent)
μ_t	turbulent viscosity
ρ	density

uniformly deployed along the length of the manifold facilitate its flow distribution function. The discharged air passes into the ambient.

The exit-flow vectors which represent the dispersing flow in Fig. 1 are schematic in that they are uniform in magnitude and direction. In practice, it is reasonable to expect that the magnitude and direction of the individual emerging streams will vary along the length of the manifold. That variation will be determined as one of the outcomes of this investigation.

As has already been discussed, the present research will include two synergistic parts. One part is numerical simulation in which several turbulence models will be employed. The second part is laboratory experiments performed to obtain data to be used to identify the most appropriate turbulence model.

2. Experimental investigation of flow in a slotted perforated pipe

To facilitate the experimental work, a variable-capacity air bench consisting of four centrifugal blowers arranged in parallel was assembled. The output of the air bench exhausted into a 2-in ID (5.08 cm), 5 feet-long (152.4 cm) PVC pipe which conveyed the air to the inlet of the test section. The test section consisted of an instrumented circular pipe having an inner diameter of 1.76 in. (4.47 cm), an outer diameter of approximately 2 in. (5.08 cm), and an overall length of 10 feet (304.8 cm). At its upstream end, the test section mated smoothly with the downstream end of the PVC air-delivery pipe.

The test section encompassed three sequential zones starting with a hydrodynamic development length of 25 feet (762 cm), a length of 21 feet (640.1 cm) where the flow was fully developed, and a 2.5 feet-long manifold (76.2 cm) having 39 slot-like apertures through which the air passed into the surrounding environment. The apertures were approximately rectangular in shape with an axial dimension of 0.625 in. (0.159 cm) and width 0.0625 in. (0.0159 cm). Each aperture was axially spaced 0.125 in. (0.318 cm) from its neighbor. A photograph of a representative aperture is presented in Fig. 2.

Fig. 2. Photograph of a representative aperture in the array of 39 exit apertures.

The objective of the experiments was to determine the axial distribution of pressure in the manifold. This information is parameterized by the Reynolds number. Both the measurement of the pressure distribution and the determination of the volumetric flowrate, necessary for the evaluation of the Reynolds number, were facilitated by installation of pressure taps. The geometry of the pressure taps is illustrated in Fig. 3. As seen in the figure, the

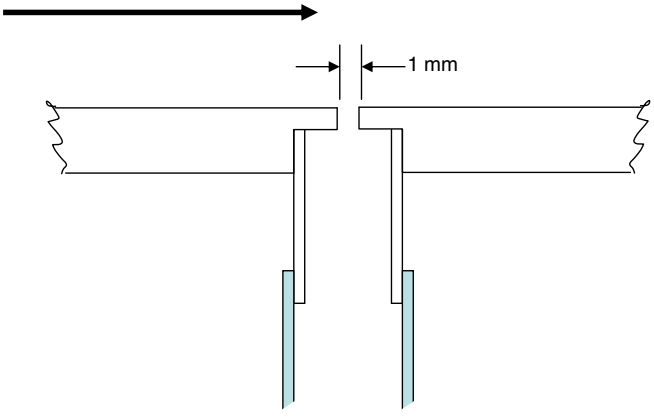

Fig. 3. Pressure tap geometry.

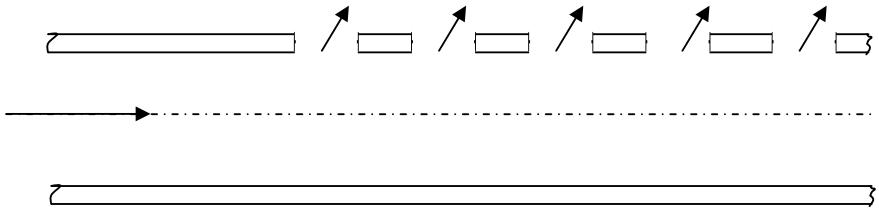

Fig. 1. Schematic diagram of a distribution manifold with air discharging into ambient.

actual tap hole was selected to have a diameter of 1 mm. This dimension was chosen on the basis of prior experience in which a given pressure was measured by means of a sequence of tap holes of different diameters.

Nine uniformly spaced pressure taps were installed along the length of the section of pipe in which fully developed flow prevailed. The inter-tap spacing was 8.75 in. (25.23 cm). These taps provided the expected linear pressure variation, and the resulting pressure gradient was used to deduce the volumetric flowrate as will be discussed shortly.

The deployment of the pressure taps in the manifold is illustrated in Fig. 4. As seen there, the pressure taps were installed at axial locations centered at the midpoint of every-other aperture. This resulted in an inter-tap spacing of 1.500 in. (3.81 cm).

At each axial station at which a tap was installed, it was positioned at a circumferential location that is 180° from its respective aperture. The choice of the circumferential positioning of the pressure taps was made to ensure that the tap reliably measured the static pressure of the nearby fluid. It is well known that wall pressure taps are a reliable means of measuring fluid static pressure when the streamlines of the flow are strictly parallel to the wall. In the present situation, it is unlikely that strict parallelism prevailed anywhere in the manifold. The closest approach to streamline parallelism would be expected to occur at locations remote from the exit apertures. The circumferential location displaced by 180° from an exit aperture is the most remote possible location for a pressure tap.

The readings of the pressure taps was accomplished by means of a U-tube manometer. One leg of the manometer received the pressure signal from a selected tap, while the other leg was open to the atmosphere. The pressure differences that were measured in this way were sufficiently large (~20 in. of water column) so that the use of a simple manometer was sufficient to achieve excellent accuracy. The individual readings were made to within 1/32 in.

As mentioned earlier, it was necessary to measure the volumetric flow rate in order to evaluate the Reynolds number. Two independent methods were used to determine the flow rate. One of the methods was based on the measurement of the axial pressure gradient in the fully developed flow, and the other method made use of a Pitot tube. These methods will now be described in some detail.

Suppose that the axial pressure gradient (dp/dx) in the fully developed flow is measured and found to be linear. Also, the density ρ of the fluid in the fully developed region is readily determined, for example, by means of the ideal gas law. The fluid viscosity μ may be obtained from a table look-up. The starting point of the analysis is the definition of the friction factor f, which is stated in Eq. (1) below. In that equation, the symbols D and U, respectively, denote the inside diameter of the pipe and the mean velocity. Note that both f and U, as they appear in Eq. (1), are unknown. A second relationship between f and U is obtained by

$$f = \frac{(-dp/dx)D}{(1/2)\rho U^2} \tag{1}$$

making use of a widely accepted algebraic correlation of the friction factor with the Reynolds number [15].

$$f = \left(\frac{1}{[1.8\log_{10}(Re/6.9)]}\right)^2 \tag{2}$$

where

$$Re = \rho UD/\mu \tag{3}$$

Eqs. (2) and (3), taken together, provide a second relationship between f and U. Furthermore, the set of Eqs. (1)–(3) provides a means of determining the velocity U corresponding to the measured pressure gradient (dp/dx).

The second method of determining the mean velocity U makes use of a Pitot-static tube. Specifically, the Pitot tube measurement provides the value of the maximum velocity U_{max} at a representative cross-section in the fully developed region. This measurement is especially convenient because it does not require a traverse in which careful accounting has to be made of the location of the sensing tip of the Pitot tube. All that is required is to traverse the tube until a maximum reading is found. Next, a relationship connecting U_{max} and U is needed. For a fully developed turbulent flow in a pipe, there are, at least, two well known such relationships. One of these appears in the treatise by Schlichting [16]. That relationship is based on the power-law representation of the turbulent velocity profile in a pipe. The other relationship [15] is more contemporary and is believed to be more accurate. It is

$$U_{max}/U = 1 + 1.33\sqrt{f} \tag{4}$$

where the Reynolds number is given by Eq. (3). Taken together, the Eqs. (3) and (4) constitute an equation for U which can be readily solved by iteration.

These two independent methods of determining U were found to provide numerical values that were in agreement to within 2–3%. Once the value of U had been determined, it was used to evaluate the Reynolds number of the slot-free delivery pipe from Eq. (3). The data runs were parameterized by that Reynolds number.

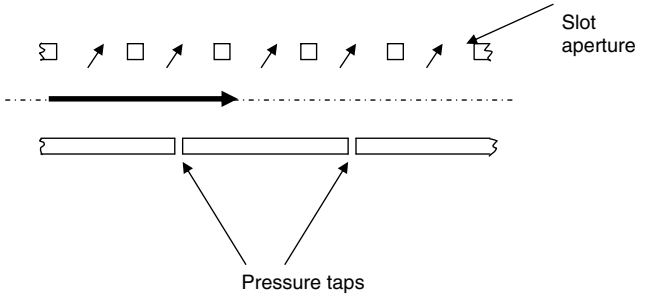

Fig. 4. Deployment of pressure taps in the manifold.

3. Governing equations for turbulent flow in a pipe

The starting point of the analysis is the Reynolds-averaged, Navier–Stokes (RANS) equations. For incompressible, constant-property flow, these equations are

x-momentum:

$$\rho\left[\frac{\partial}{\partial x}(u^2) + \frac{\partial}{\partial y}(uv) + \frac{\partial}{\partial z}(uw)\right] = -\frac{\partial p}{\partial x} + \frac{\partial}{\partial x}\left(\mu_{eff}\frac{\partial u}{\partial x}\right) + \frac{\partial}{\partial y}\left(\mu_{eff}\frac{\partial u}{\partial y}\right) + \frac{\partial}{\partial z}\left(\mu_{eff}\frac{\partial u}{\partial z}\right) \tag{5}$$

y-momentum:

$$\rho\left[\frac{\partial}{\partial x}(vu) + \frac{\partial}{\partial y}(v^2) + \frac{\partial}{\partial z}(vw)\right] = -\frac{\partial p}{\partial y} + \frac{\partial}{\partial x}\left(\mu_{eff}\frac{\partial v}{\partial x}\right) + \frac{\partial}{\partial y}\left(\mu_{eff}\frac{\partial v}{\partial y}\right) + \frac{\partial}{\partial z}\left(\mu_{eff}\frac{\partial v}{\partial z}\right) \tag{6}$$

z-momentum:

$$\rho\left[\frac{\partial}{\partial x}(wu)+\frac{\partial}{\partial y}(wv)+\frac{\partial}{\partial z}(w^2)\right] = -\frac{\partial p}{\partial z}+\frac{\partial}{\partial x}\left(\mu_{\text{eff}}\frac{\partial w}{\partial x}\right)+\frac{\partial}{\partial y}\left(\mu_{\text{eff}}\frac{\partial w}{\partial y}\right)+\frac{\partial}{\partial z}\left(\mu_{\text{eff}}\frac{\partial w}{\partial z}\right) \quad (7)$$

In these equations, u, v, and w are the velocity components, x, y, and z are the Cartesian coordinates, ρ is the density, and μ_{eff} is the effective viscosity defined as

$$\mu_{\text{eff}} = \mu + \mu_{\text{t}} \quad (8)$$

where μ is the molecular viscosity and μ_{t} is the so-called turbulent viscosity. In the vast majority of turbulence models, the turbulent viscosity μ_{t} is regarded as isotropic.

3.1. Turbulence models

There are a number of turbulence models available in the literature. The first of these models was created in 1974 by Launder and Spalding [14]. Their model was based on calculating the turbulence kinetic energy k and the turbulence dissipation function ε. Each of these functions is assumed to obey a conservation-type equation involving both convection and diffusion. In addition, each of the equations contains source and sink terms which represents generation and dissipation of turbulence. These equations for k and ε are partial differential equations spanning the same coordinate space as the RANS equations themselves. Since the model utilizes two additional equations beyond the RANS equations, it is called a two-equation turbulence model. The turbulent viscosity μ_{t} is determined from the computed value of k and ε by using the relation

$$\mu_{\text{t}} = C_\mu \rho \frac{k^2}{\varepsilon} \quad (9)$$

The quantity C_μ is an adjustable constant. In fact, the model encompasses a total of four adjustable constants. The values of these constants were determined by fitting predictions based on the model with experimental velocity data for relatively simple flows.

Two other turbulence models were employed here: renormalized group k–ϵ model (*RNG*) and realizable k–ϵ (*REAL*). In common with the original k–ϵ model, both the *RNG* and *REAL* models involve the solution of two additional partial differential equations which are added to the basic conservation laws for mass, momentum, and energy. These additional equations have an overall structure that is similar to that already discussed for the original k–ϵ model, but with significant differences in detail. All of the models provide a turbulent viscosity, μ_{t}, which is isotropic.

The realizable k–ϵ (REAL) is a variant of the original in which the changes allow certain mathematical constraints to be obeyed which are purported to improve the predicted end results compared with experimental data for situations of greater complexity than can be handled by the standard model. The RNG-based k–ϵ model is derived by a method somewhat different from that used in the derivation of the original k–ϵ and REAL methods. Instead of the RANS equations, the model is based on a different averaging technique called the "renormalized group" method. The outcome is a pair of transport equations for k and ϵ which contain terms and functions additional to those of the original k–ϵ model. These models contain other constants, different from those of the original k–ϵ model, which were also determined by fitting experimental data.

It is natural to start with the original k–ε model because of its many successes. The axial pressure variations predicted with the use of this model were compared with the data obtained from the experiments described earlier in the chapter. The comparison showed generally good agreement, but differences in details were observed. However, since the level of agreement was satisfactory, it seemed reasonable to seek improvements using the advances that have been made in the original model – the RNG and REAL models. The comparisons between the results predicted by these models and the data will, as demonstrated shortly, provide a definitive conclusion about which is most suitable for the analysis of the flow under consideration.

4. Results

4.1. Axial pressure variations and turbulence model selection

The first focus in the presentation of the results is to bring together the experimental data for the axial variation of the pressure with the predictions from the numerical simulations. This information is conveyed in Fig. 5. The specific Reynolds number for this figure is 110,400. The vertical axis is the difference between local pressure and the ambient pressure, while the horizontal axis represents the axial distance measured from a reference point just upstream of the first slot. The experimental data are shown as discrete square symbols. In contrast, the numerical predictions are represented by continuous curves.

Inspection of the figure reveals that among the three candidate simulation models, that which uses the Realizable k–ε model (REAL) provides the closest congruence with the data. The other two models, respectively, based on the original k–ε model (KE) and the renormalized group k–ε model (RNG), are mutually reinforcing but lie higher than both the data and the REAL predictions. On this basis, it appears reasonable to select the REAL model for future calculations involving distribution manifolds of the type being investigated.

The REAL model was employed to obtain results for a range of Reynolds numbers of practical interest. In addition to the *Re* of 110,400, computations were performed for *Re* of 40,000 and 200,000. With a view to generalizing these results, a dimensionless representation was made. In particular, instead of plotting $(p - p_{\text{amb}})$, the quantity

$$\frac{p - p_{\text{amb}}}{\frac{1}{2}\rho U^2} \quad (10)$$

will be plotted. In this definition, U is the mean velocity in the portion of the pipe that is upstream of the distribution manifold. This dimensionless presentation is conveyed in Fig. 6. The abscissa is, again, the axial distance measured downstream from a point just before the first slot. Examination of the figure reveals remarkable correlation among the curves for the various Reynolds numbers.

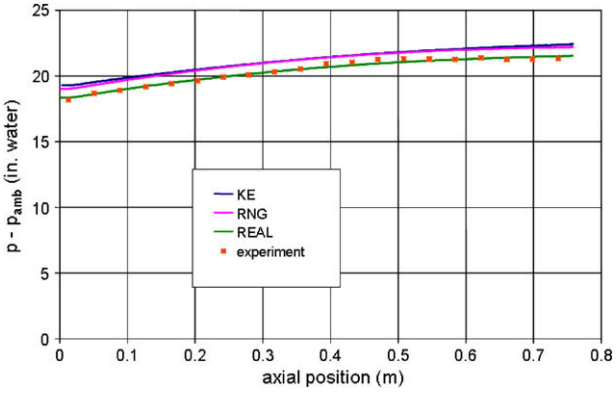

Fig. 5. Comparison of numerically predicted axial pressure distributions with experimental data for *Re* = 110,400. The turbulence models used for the predictions are the standard k–ε model (KE), the renormalized group k–ε model (RNG), and the realizable k–ε model (REAL).

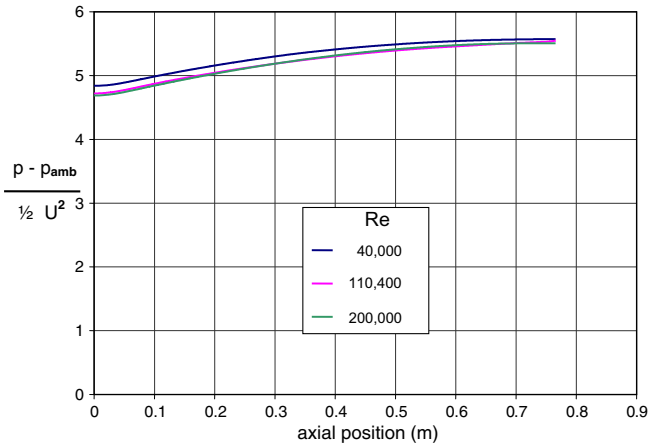

Fig. 6. Dimensionless presentation of the axial pressure distribution. The nondimensionalization is based on the velocity head of the fully developed flow upstream of the distribution manifold.

In fact, for all practical purposes, it is reasonable to regard the overlaying curves as a single universal curve that may be used within the Reynolds number range from 40,000 to 200,000. Furthermore, in view of the tight packing of the curves, moderate extrapolation outside of this range is believed permissible.

4.2. Per-slot mass flow discharge

In view of the successful correlation displayed in Fig. 6, other results from the numerical solutions were examined with regard to whether or not they might also be universal. Among the results of practical interest is the possible axial variation of the individual mass flow rates emanating from each of the slots. The normalized mass flow rate per slot is plotted in Fig. 7 as a function of the axial distance along the manifold. The normalized per-slot mass flow rate is defined as

$$m^*_{slot}/m^*_{avg} \tag{11}$$

where the numerator is the per-slot value and the denominator is the total mass flow rate divided by the number of slots. The use of this normalization is a useful form in that it indicates the deviation of the individual mass flow rates from the average value.

Fig. 7 shows that the expected correlation of the results does, indeed, occur. The normalization defined by Eq. (11) virtually eliminates the Reynolds number dependence. Of equal interest is the axial variation of the per-slot mass flow rate. As seen in the figure, the smallest outflows occur near the beginning of the manifold.

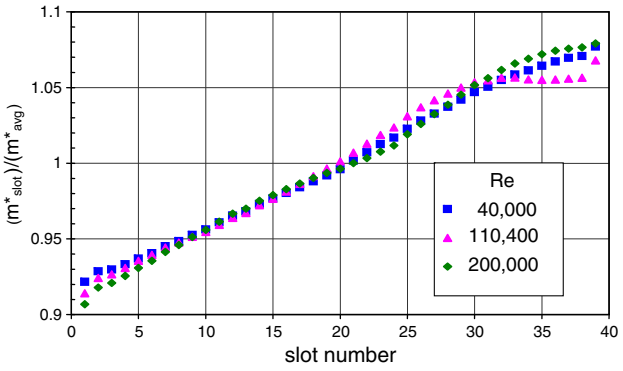

Fig. 7. Nondimensional presentation of the axial distribution of the per-slot mass flow rate. The denominator is the average per-slot flow rate.

With increasing downstream distance, the per-slot mass flow rate increases monotonically, achieving a maximum value at the downstream end. This behavior is consistent with the pressure distributions that have been displayed in Figs. 5 and 6. These figures show that the local-to-ambient pressure differences increase with increasing downstream distances. Since it is that pressure difference which drives the per-slot mass flow rate, it is necessary that flow rate also increases with downstream distance.

Further examination of Fig. 7 reveals that the end-to-end variation in the per-slot mass flow rate is approximately 18%, with a swing of about ±10% around the mean. The importance of this variation has to be judged by the application in question. For example, if the jets created by the outflow from the manifold were to serve to cool a hot surface by means of impingement, it is expected that the variation of the corresponding heat transfer coefficients along the surface would not exceed 18%. For sensitive applications, variations of this magnitude might be judged to be unacceptable.

It is interesting to compare the end-to-end pressure variation from Fig. 5 with the variation of the per-slot mass flow rate from Fig. 7 for $Re = 110{,}400$. The pressure variation was found to be 15.7% while the flow rate variation was 15.5%. These virtually identical variations provide strong evidence of the dominant role of the interior-to-exterior pressure difference in determining the outflows through the respective slots. This comparison was made for the specific Reynolds number for which data were collected. However, in view of the universal nature of the normalizations displayed in Figs. 6 and 7, the foregoing conclusion applies to all Reynolds numbers in the investigated range from 40,000 to 200,000.

4.3. Air discharge angles

Another result of practical interest is the angles at which the air is discharged from the exit slots. This information was obtained experimentally and from numerical simulations. The experimental setup will be described first with the aid of Fig. 8. The figure depicts a portion of the manifold showing the air discharge slots and the setup for implementing oil-lampblack technique. As can be seen, a shelf-like structure was put in place perpendicular to the surface of the manifold and positioned just below the exit slots. The shelf was covered with white contact paper. Prior to the initiation of the air flow, a dot of the oil-lampblack mixture was carefully placed at the longitudinal center of each slot, at the point where the shelf intersects the surface of the manifold pipe. The activation of airflow caused the mixture to move outward along the shelf as illustrated in the figure. At the conclusion of the experiment, the streaks were photographed and, subsequently, the angles of the departure of the discharging air were read. The departure angle is defined as the angle of the streakline traced by the mixture with respect to the axis of the manifold. Experimental data were collected for two Reynolds numbers, approximately 110,000 and 140,000.

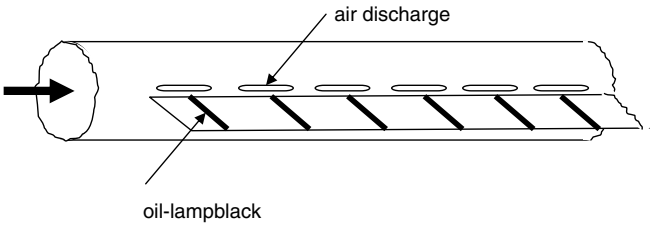

Fig. 8. Experimental setup for flow visualization by means of the oil-lampblack technique.

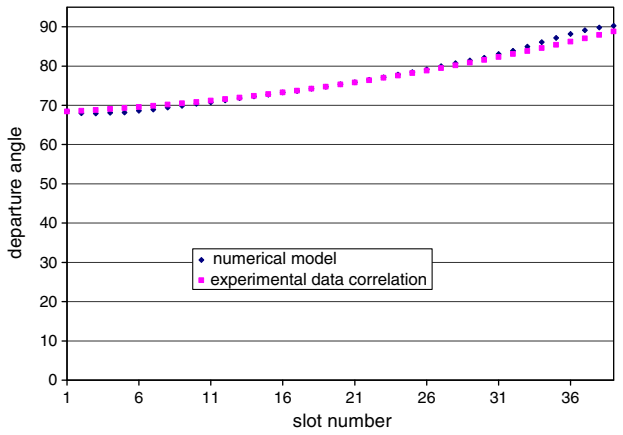

Fig. 9. Slot exit air discharge angle comparison between data and model for a Reynolds number of approximately 110,000.

The experimental data were correlated by means of a least-square fit which yielded the equation

$$\text{departure angle} = 0.009207n^2 + 0.1687n + 68.23 \qquad (12)$$

where n is the slot number, with $n = 1$ being the most upstream slot. The correlation as defined by Eq. (12) is plotted as the square symbols in Fig. 9. Also shown in the figure is the result obtained from the numerical simulation. The latter results are represented in the figure by the diamond symbol. Comparison of the two sets of results in Fig. 9 shows excellent agreement between the experimental data and numerical results. The quality of the agreement lends support to the selected turbulence model as well as the numerical technique.

Further inspection of Fig. 9 shows that the departure angles progress smoothly from a value that is approximately 70° relative to the axis to a value that is essentially 90° with respect to the axis. The latter angle corresponds to perpendicular exhaust from the manifold. This behavior can be explained by considering the axial momentum carried by the air flowing in the bore of the manifold. At locations just downstream of the manifold inlet, the air flow is unidirectional so that its momentum is purely axial. As the flow proceeds in the downstream direction, the axial momentum decreases monotonically. Consequently, the axial component of the flow discharging from the slots is greatest near the upstream end of the manifold. The just-described diminution of the axial momentum is reflected in the discharging jets, with the result that the departure angles are less and less inclined to the perpendicular. At the very downstream end of the manifold, the axial momentum is fully depleted and the discharging flow is precisely perpendicular to the axis.

To complement the foregoing presentation of jet-departure angles, a contour diagram, Fig. 10, has been prepared. These results correspond to a Reynolds number of approximately 110,000. In that diagram, the colors are coded according to the velocity magnitude in m/s. Inspection of the diagram reveals a systematic evolution of the departure angle from an oblique direction to the perpendicular direction. This change in departure angle is related to the decrease of the axial momentum as the flow proceeds from the inlet to farther downstream locations. Also in evidence is a broadening of the jet with increasing downstream distance. A more careful observation discloses a zone of relatively slow flow in the space between the successive jets. With increasing downstream distance, this inter-jet flow appears to grow somewhat more vigorous.

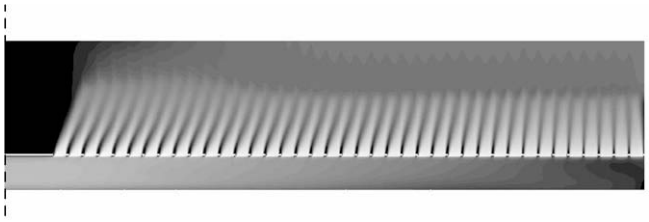

Fig. 10. Velocity contour diagram showing the inclinations of jets departing from the manifold.

More detailed information about the patterns of fluid flow in the region of jet departure is provided in Fig. 11(a) and (b). That figure is a composite of the flow patterns at exit ports 1 and 39. It is readily seen that there are significant differences in the manner in which the fluid emerges from the ports depending on the location with respect to the inlet of the manifold. Near the inlet, at port number 1, the exiting air possesses a significant amount of axial momentum which causes the jet to have a downstream inclination. Furthermore, at that port location, local variations in the departure angle across the streamwise length of the slot can be seen. Also, the degradation of the jet stream due to interaction with the surroundings occurs rather rapidly. In contrast, at port number 39, there is no evidence of any axial momentum carried by the emerging jet. The jet is purely radial. The outflow through port number 39 is characterized by a uniform departure angle and a uniform velocity magnitude. The uniformity of the velocity persists to a significant distance from the port proper.

The observations that were made in the preceding paragraph reinforce the findings that were identified in Figs. 7 and 9. In Fig. 7, it was seen that the strength of the jet, as indicated by the per-port mass flow rate, is least at port number 1 and greatest at port number 39. This characteristic explains the different rates of degradation of the emerging jets at those locations.

5. Mesh independence and solution domain

In any numerical simulations, it is necessary to establish accuracy by investigating the dependence/independence of the results from the specifics of the solution domain and of the number and deployment of the control volumes.

5.1. Mesh independence

In the conventional treatment of mesh independence, primary focus is directed to the numbers of elements, control volumes, or nodes. While this approach is useful, it is not a complete inquiry of the issue of mesh independence. It is believed that the matter of mesh deployment is of equal importance to the numbers of constituents of the mesh. Here, the mesh independence study will include both numbers and deployment.

The original structure of the mesh was based on intuition accumulated over a number of years of involvement with the numerical simulations of fluid flow. To illustrate the nature of the originally constructed mesh, Figs. 12 and 13 have been prepared. It can be seen that the control volumes of the mesh are hexahedral. Note also that the mesh is more densely deployed in the neighborhood of walls in order to resolve the high gradients that are expected to occur in those regions. It is also noteworthy that the mesh is neatly aligned along the respective coordinate directions. The meshing tool used to accomplish the meshing is ICEM, an advanced, commercially available software package.

Figs. 12 and 13 correspond, respectively, to the finer and sparser meshes that were employed in the study. The respective numbers of control volume for these meshes are 1,695,700 and 236,600.

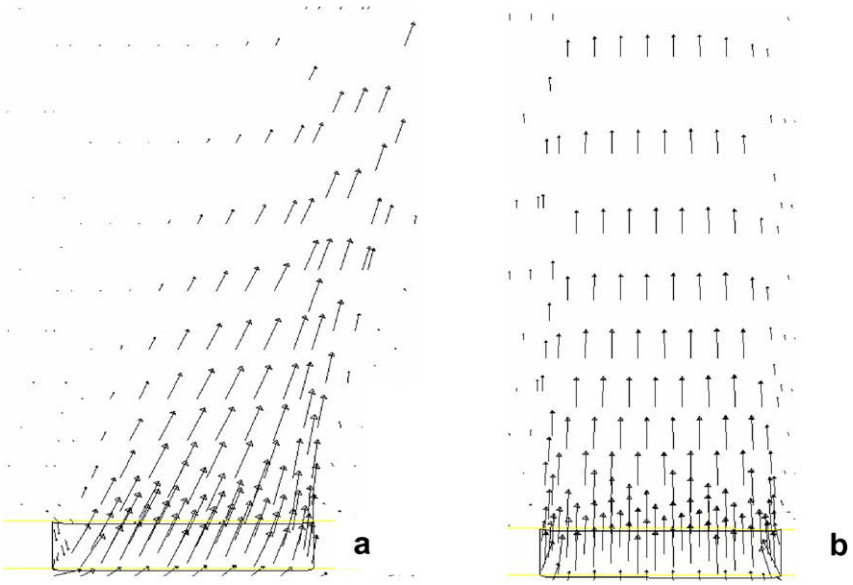

Fig. 11. Details of the flow field of the jets exiting from ports 1 (part a) and 39 (part b).

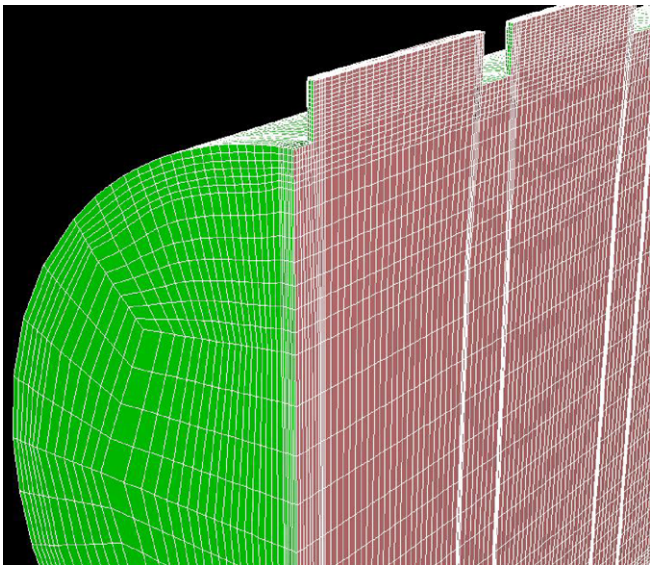

Fig. 12. Illustrative portion of the finer mesh used for the numerical simulation. The total number of control volumes for this mesh is 1,695,700. The illustrated portion shows the diametral plane and the end face of half of the manifold cross-section.

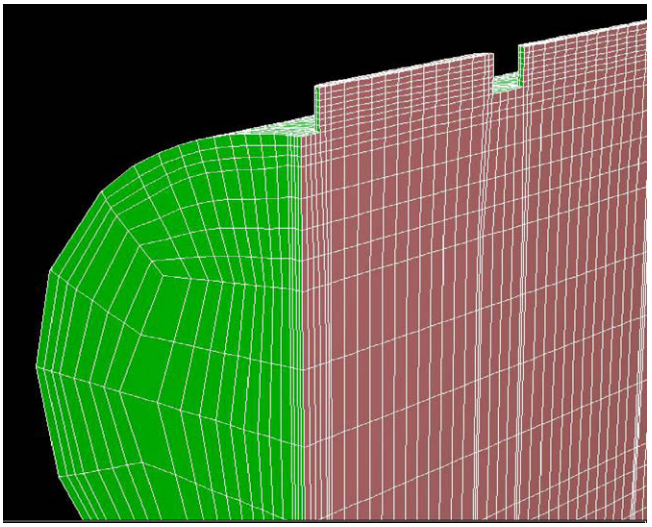

Fig. 13. Illustrative portion of the sparser mesh used for the numerical simulation. The total number of control volumes for this mesh is 236,600.

For the mesh independence study, the original (finer) mesh was modified by using a uniform reduction of the number of control volumes in each subdivision of the original mesh. The result of this process yielded the sparser mesh for which the number of control volumes is 1/8 of that of the original.

To examine the mesh independence issue, attention is focused on one of the key results of the simulations – the per-slot distribution of the mass flow rate exiting the manifold. This issue has been examined as a function of the Reynolds number in Fig. 7, where it was shown to be essentially independent of the Reynolds number. In this light, it was deemed sufficient to confine the mesh independence study to the intermediate Reynolds number, approximately Re = 110,000. The results of the mesh independence study are presented in Fig. 14 in which the normalized distribution of the per-slot mass flow rate is plotted as a function of the slot number. The figure contains the results for the original mesh (the dense mesh) and the reduced mesh (the sparse mesh). Inspection of the figure reveals outstanding agreement between the results for the two meshes. This agreement looms even larger when it is recognized that the two meshes are populated by numbers of control volumes that differ by a factor of eight. On this basis, it may be concluded that the results do not depend upon the specifics of the mesh.

5.2. Solution domain

In many problems of fluid flow, the geometry and size of the solution domain is more or less obvious. However, in instances such as that being considered here, there is some ambiguity in the selection of the proper solution domain. Specifically, the jets that effuse from the various exit slots pass freely into the environment without constraint. The extent of the influence of the flow in the environment on the flow internal to the manifold is uncertain. To examine this issue, the solution domain was

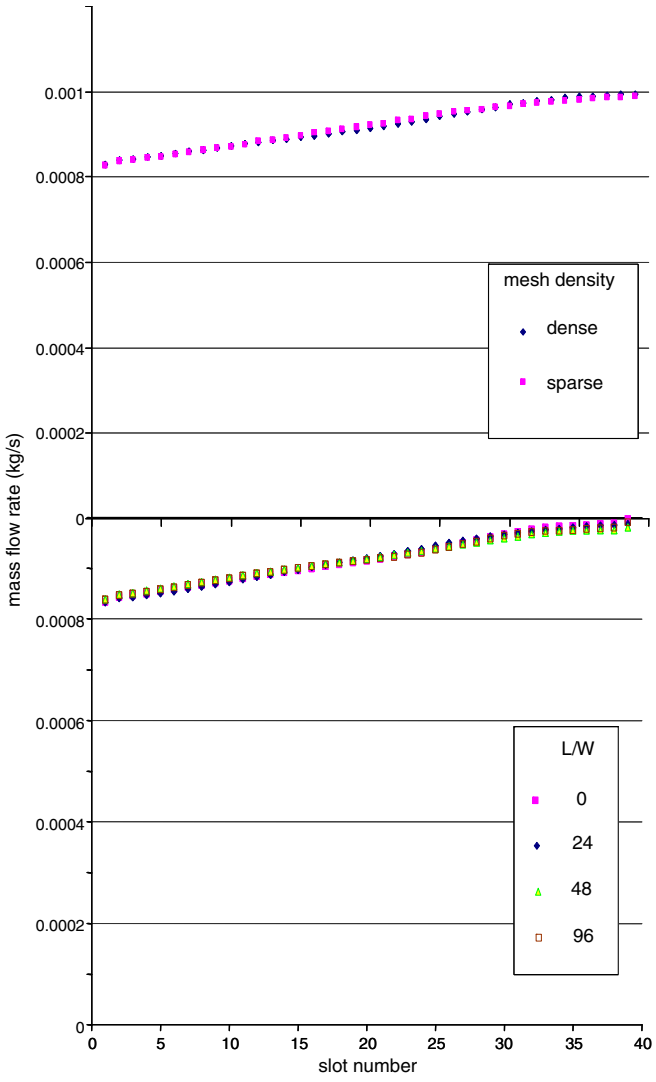

Fig. 14. Mesh independence study for $Re = 110{,}000$.

extended outward from the outer surface of the manifold into the surrounding space. Four different extended domains are considered. In one of these, to be regarded as a baseline case, the solution domain is drawn tightly against the outer surface of the manifold. Therefore, the solution domain for this case does not extend into the surroundings. The first extended domain is characterized by the ratio of $L/W = 24$, where L is the radial distance from the outer surface of the pipe to the downstream boundary of the solution domain and W is the slot width. The third and fourth solution domains had L/W values of 48 and 96, respectively. The angle subtended by the downstream boundary of the solution domain is 20°. The calculations for this study were performed for $Re = 110{,}000$.

The distribution of the per-slot outflows will be used in the assessment of the impact of the size of the solution domain. These results are conveyed in Fig. 14. The figure indicates a remarkable insensitivity to the size of the solution domain. In fact, it appears that there is no difference between the results obtained with a domain which does not extend into the surroundings and a domain which is extended. This outcome is very advantageous from the standpoint of actual computation, since the absence of the extended solution domain diminishes the number of control volumes needed to execute the solution.

5.3. Near-wall treatment

The deployment of nodes in the region adjacent to the bounding walls of a flow is a major issue which is thought to impact the accuracy of the numerical results. This is especially true when the flow is turbulent. In the near wall region of a turbulent flow, the degree of turbulence is of lesser magnitude than far from the wall. There are two primary approaches to recognize this change in turbulence level. One is to reformulate the governing equations for the production and dissipation of turbulence to make them applicable to the physical phenomena which occur near the wall. An alternative is to seek a means for bridging between the wall and the region away from the wall where full turbulence intensity exists. This latter approach is commonly termed the *wall-function* method [14]. For the present numerical simulation, the wall-function method is utilized.

The wall functions are algebraic relationships that are based on the so-called universal velocity distribution [17]. These relationships, initially based on experimental data for simple flow such as round pipes and boundary layers, connect a dimensionless velocity with a dimensionless distance from the wall. In its original form, the equation for the near-wall portion of the universal velocity profile is expressed in logarithmic terms.

6. Concluding remarks

The fluid flow in manifolds includes many features which distinguish it from conventional wall-bounded flows. In particular, for a distribution manifold, there is a periodic branching and turning of the flow as it encounters the successive exit apertures. The exiting streams give rise to transverse flows and to a severe depletion of the axial momentum of the mainflow. In practice, manifold flows in practical devices such as heat exchangers are turbulent. In view of the aforementioned complexities and others, it is unwise to base numerical simulations of such flows on a casual selection of a turbulence model.

These considerations motivated a study which encompassed careful numerical simulations and painstaking experiments, both performed in-house. The experimental results were used to judge the suitability of the various turbulence models. Although the selection process was based on the capability of the simulations to represent the experimentally determined axial pressure distribution, the validity of this process was confirmed by the superb agreement of the simulation-based and experiment-based departure angles at the respective exit ports.

The reported results included not only the axial pressure distributions and the departure angles, but also the per-exit-port mass flow. In practice, the efficacy of a distribution manifold is based on the degree of uniformity of the per-port fluid efflux. Both the axial pressure drop results and the mass-efflux results were reported in dimensionless forms which eliminated their dependence on the Reynolds number.

References

[1] I. Ieronymidis, D.R.H. Gillespie, P.T. Ireland, R. Kingston, Experimental and computational flow field studies of an integrally cast cooling manifold with and without rotation, in: Proceedings of the 51st ASME Turbo Expo, vol. 3, Part B, 2006, pp. 1041–1053.
[2] B. Xu, F. Liang, S. Lai, Numerical analysis and visualization of natural gas jet with multi-point injection system, Chin. J. Mech. Eng. 18 (2005) 550–554.
[3] S.C. Kale, V. Ganesan, Investigation of the flow field in the various regions of intake manifold of a S.I. engine, Indian J. Eng. Mat. Sci. 11 (2004) 85–92.
[4] R. Milanovic, CFD modeling of flow and heat transfer inside a liquid-cooled exhaust manifold, in: Proceedings of the 2003 ASME Summer Heat Transfer Conference, vol. 3, 2003, pp. 785–792.
[5] S. Malhotra, K.P. Biswas, A.K. Vohra, B.S. Gill, S. Banik, Heater combustion air duct design and simulation, Hydrocarb. Process. 82 (2003) 53–57.

[6] U. Kresovic, CFD analysis of liquid-cooled exhaust manifolds in a real engine cycle, Proc. ASME Heat Transfer Div. 372 (4) (2002) 39–46.
[7] T. Bissinger, M. Lepel, Flow field investigations in intake manifolds of industrial gas turbines including CFD matching, VDI Berichte 1721 (2002) 107–114.
[8] L. Sclafani, L. Postrioti, Numerical analysis of a fluid flow in a racing motorcycle intake system, in: Proceeding of the IASTED International Conference, June 2002, Crete, Greece.
[9] G.F. Jones, J.M. Galliera, Isothermal flow distribution in coupled manifolds: comparison of results from CFD and an integral model, Proc. ASME Fluids Eng. Div. 247 (1998) 189–195.
[10] A. Huser, O. Kvernvold, Prediction of sand erosion in process and pipe components, BHR Group Conf. Ser. Publ. 38 (1998) 217–227.
[11] T.-W. Kuo, D.L. Reuss, Multidimensional port-and-cylinder flow calculations for the transparent-combustion-chamber engine, Proc. ASME Intern. Combust. Eng. Div. 23 (1995) 19–29.
[12] A.E. Holdo, S.J. Wakes, K. Mallone, Mesh grading in the near wall region when modeling transient turbulent flows, Proc. ASME Fluids Eng. Div. 216 (1995) 1–6.
[13] X.A. Wang, P. Yu, Isothermal flow distribution in header systems, Int. J. Solar Energy 7 (1989) 159–169.
[14] B.E. Launder, D.B. Spalding, Numerical computation of turbulent flows, Comp. Meth. Appl. Mech. Eng. 3 (1974) 269–289.
[15] F.M. White, Fluid Mechanics, fifth ed., McGraw-Hill, New York, 2003.
[16] H. Schlichting, Boundary-Layer Theory, seventh ed., McGraw-Hill, New York, 1979.
[17] F.M. White, Viscous Fluid Flow, third ed., McGraw-Hill, New York, 2006.